

# Operation of a high-frequency, phase-slip qubit

Cheeranjeev Purmessur,<sup>1</sup> Kaicheung Chow,<sup>2</sup> Bernard van Heck,<sup>3</sup> and Angela Kou<sup>1,2,4</sup>

<sup>1</sup>*Department of Physics, University of Illinois Urbana-Champaign, Urbana, IL 61801*

<sup>2</sup>*Holonyak Micro & Nanotechnology Lab, University of Illinois Urbana-Champaign, Urbana, IL 61801*

<sup>3</sup>*Dipartimento di Fisica, Sapienza Università di Roma, 00185 Roma, IT*

<sup>4</sup>*Materials Research Laboratory, University of Illinois at Urbana-Champaign, Urbana, IL 61801*

(Dated: February 12, 2025)

Aluminum-based Josephson junctions are currently the main sources of nonlinearity for control and manipulation of superconducting qubits. A phase-slip junction, the dual of a Josephson junction, provides an alternative source of nonlinearity that promises new types of protected qubits and the possibility of high-temperature and high-frequency operation through the use of superconductors with larger energy gaps. Phase-slip junctions have been challenging, however, to incorporate into superconducting qubits because of difficulty controlling junction parameters. Here we demonstrate the operation of a superconducting qubit based on a phase slip junction made using titanium nitride. We operate the qubit at zero flux where the qubit frequency ( $\sim 17$  GHz) is mainly determined by the inductance of the qubit. We perform readout and coherent control of the superconducting qubit, and measure qubit lifetimes  $> 60 \mu\text{s}$ . Finally, we demonstrate operation of the qubit at temperatures exceeding 300 mK. Our results add the phase-slip junction as a tool for superconducting quantum information processing and opens avenues for new classes of superconducting qubits.

Josephson junctions (JJ) are the primary source of non-linearity for superconducting circuits. The JJ acts as a non-linear inductor when incorporated into a circuit and has led to the creation of a multitude of useful quantum devices such as quantum-limited amplifiers, single-photon detectors, and superconducting qubits [1–5]. The dual of a JJ, a phase-slip junction (PSJ), acts as a non-linear capacitor and would greatly expand the superconducting circuit toolbox. Proposals envision building PSJ-based qubits with stronger anharmonicities than their JJ-based counterparts [6], phase-slip oscillators that are highly sensitive and tunable via parametric drives [7], and a current standard based on quantum phase slips [8]. Despite these proposed benefits, the PSJ has only been used in a handful of experiments [9–16]. This is in part due to the difficulty with fabricating a PSJ, which is formed from a strip of superconductor narrower than its coherence length. Recent experiments have started to incorporate PSJs into quantum interference devices [15] and into circuits that could be used for metrology [16].

Incorporating PSJs into qubits would be particularly beneficial for quantum information processing. The operating principle of PSJ-based qubits is predicated on flux quanta tunneling through the PSJ to create qubit states that are superpositions of persistent-current states [6]. Such qubit states are similar to those used in the fluxonium [17], the bifluxon qubit [18], and the  $0-\pi$  qubit [19, 20], but created without capacitors in the qubit circuit. This is useful since capacitors lead to increased sensitivity to charge-based noise sources as well as spurious modes that limit the operating frequency range and control mechanisms of the above-mentioned qubits. Additionally, PSJ-based qubits can be made from single films of higher-energy gap superconductors than aluminum. These qubits could have transition frequencies higher than those of current superconducting qubits, which would enable qubit operation above dilution re-

frigerator temperatures and would ease signal transduction between superconducting qubits and higher-energy quantum communication platforms such as optical photons. Finally, it has been proposed that combining a phase slip junction with a Josephson junction in a qubit could lead to a robust noise-protected qubit [21]. It has been singularly challenging, however, to build PSJ-based qubits [9, 11]. Qubit frequencies could not be determined through design [9], and qubit coherence times were only inferred by spectroscopic linewidths [11].

In this work, we demonstrate the operation of a high-frequency superconducting qubit based on a PSJ. We fabricate the qubit using a single thin film of titanium nitride (TiN). The qubit is biased to zero flux where the qubit basis states are similar to the recently-demonstrated bifluxon qubit [18, 22, 23] and the qubit frequency is mainly determined by the well-controlled qubit inductance. At this sweet spot, we demonstrate readout and coherent manipulation of the qubit. We observe qubit lifetimes in excess of  $60 \mu\text{s}$  and qubit coherence times of  $\sim 17 \text{ ns}$ . Finally, we exploit the higher energy gap of TiN to operate the qubit at temperatures  $> 300 \text{ mK}$ . The relaxation and coherence times of the qubit remain robust, with  $T_{2R}$  unchanged and  $T_1$  remaining above  $10 \mu\text{s}$ , at these temperatures.

A phase slip qubit is formed from an inductance in parallel with a PSJ, which creates a superconducting loop as shown in Fig. 1(a) [6]. The eigenstates in a continuous superconducting loop are persistent-current states that correspond to quantized flux quanta in the loop. The addition of a PSJ, where quantum fluctuations of the superconducting order parameter are large, leads to flux quanta tunneling coherently through the PSJ. This tunneling process is known as a coherent quantum phase slip (CQPS). The eigenstates of the phase slip circuit are then coherent superpositions of different numbers of flux quanta in the loop. The phase slip qubit is defined by

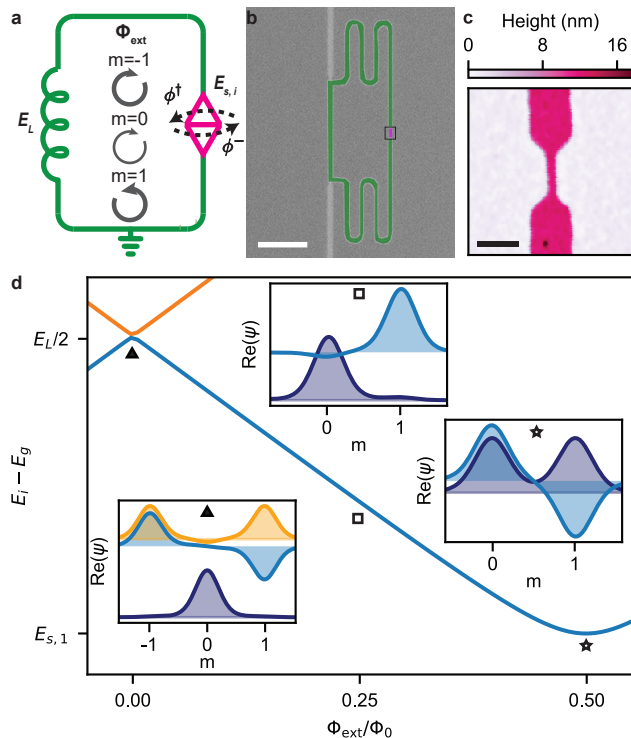


FIG. 1. **The phase-slip qubit.** (a) Circuit schematic of the device. The superinductance (green) is in parallel with a PSJ (pink) where flux quanta can tunnel into and out of the loop at a rate  $E_{s,i}$ . The arrows indicate the strength and chirality of the current in the loop for fluxon states,  $m = -1, 0, 1$  when the external flux,  $\Phi_{\text{ext}}$ , is slightly off of zero flux. (b) False-colored SEM image of lithographically similar device to Device A with the superinductance shown in green and the PSJ shown in pink. The qubit is inductively coupled to a readout resonator (light gray). Scale bar corresponds to  $5 \mu\text{m}$ . (c) Atomic force microscopy image of the 18 nm wide constriction forming the PSJ. Scale bar corresponds to 100 nm. (d) Transition energy spectrum from the ground state of a phase slip qubit as a function of  $\Phi_{\text{ext}}$ . At zero flux the qubit frequency is mainly determined by  $E_L$ , provided that  $E_L \gg E_{s,i}$ . The insets show the wavefunctions of the ground (navy), first (blue), and second excited (orange) states at  $\Phi_{\text{ext}} = 0, 0.25$  and  $0.5 \Phi_0$ .

the ground ( $|g\rangle$ ) and first excited ( $|e\rangle$ ) states of this device. By tuning the flux through the phase slip circuit,  $\Phi_{\text{ext}}$ , one can adjust the qubit energies and eigenstates as shown in Fig. 1(d). The operating principle of a phase slip qubit is similar to that of superconducting flux-based qubits based on Josephson junctions [17, 24].

Integer and half-multiple flux quantum through the phase slip qubit are particularly interesting operating points. Here, qubit eigenstates are equal superpositions of flux quanta through the loop and become insensitive to dephasing from fluctuations in the flux through the phase slip qubit. Previous implementations of the phase slip qubit have been operated at half-flux quantum [9, 11]. Half-flux quantum, however, is a difficult operating point

for phase slip qubits made using PSJs due to the exponential sensitivity of the qubit energy on the width of the constriction forming the PSJ.

We focus instead on the integer-flux operating point of the phase slip qubit. Here, the qubit energy remains insensitive to flux noise while also being only weakly dependent on the phase slip rate through the PSJ. The qubit frequency is primarily determined by  $E_L$  in the limit  $E_L \gg E_{s,i}$ , where  $E_L = \Phi_0^2/L_k$  is the energy due to the inductance ( $L_k$ ) of the loop and  $E_{s,i}$  is the rate of  $i$  coherent quantum phase slips through the PSJ. The inductive energy is controlled reliably through the inductance of the phase slip qubit.  $E_{s,i}$  determines the energy splitting between the first and second-excited ( $|f\rangle$ ) states, which is a small perturbation on the qubit frequency. At integer flux, the qubit is thus minimally sensitive to the geometric parameters of the PSJ. Moreover, the minimal overlap between the ground and excited state of the qubit eigenstates at integer flux provides increased protection against qubit relaxation [18, 22, 23].

Our implementation of a phase slip qubit is shown in Fig. 1(b)-(c). The device is formed from a single layer of thin (5 nm thick) TiN, which was chosen due to its large kinetic inductance [25–27] and high measured quality factors [25, 28]. We fabricated the PSJ from a narrow constriction of width  $\sim 18$  nm (Fig. 1(c)), which is smaller than the expected coherence length of TiN to enable CQPS through the PSJ [29]. Since phase slips across the inductance are a detrimental dephasing process for the phase slip qubit, we designed the width of the inductance to be 150 nm, which should be wide enough relative to the superconducting coherence length to prevent these spurious phase slips. The inductance is shown in green in Fig. 1(b). We couple the phase slip device inductively to a readout resonator in order to perform dispersive readout using standard circuitQED techniques [30]. We have measured two devices (A and B), which showed similar results. We will discuss Device A in the main text while measurements from Device B can be found in the Supplementary Information.

We first performed two-tone spectroscopy on the device to check that it is behaving as a phase slip qubit (Fig. 2). We expect the behavior of the device to be described by the following Hamiltonian written in the fluxon basis:

$$\begin{aligned}
 H = & \frac{E_L}{2} \sum_m \left[ \left( m - \frac{\Phi_{\text{ext}}}{\Phi_0} \right)^2 |m\rangle \langle m| \right] \\
 & - \frac{E_{s,1}}{2} \sum_m (|m\rangle \langle m+1| + |m+1\rangle \langle m|) \\
 & + \frac{E_{s,2}}{2} \sum_m (|m\rangle \langle m+2| + |m+2\rangle \langle m|)
 \end{aligned} \quad (1)$$

where  $m$  is the number of fluxons in the loop,  $E_{s,1}$  is the phase slip rate for coupling the fluxon states  $m$  and  $m+1$ , and  $E_{s,2}$  is the rate at which two flux quanta tunnel simultaneously, coupling the fluxon states  $m$  and  $m+2$ . We fit the observed transitions to the Hamiltonian

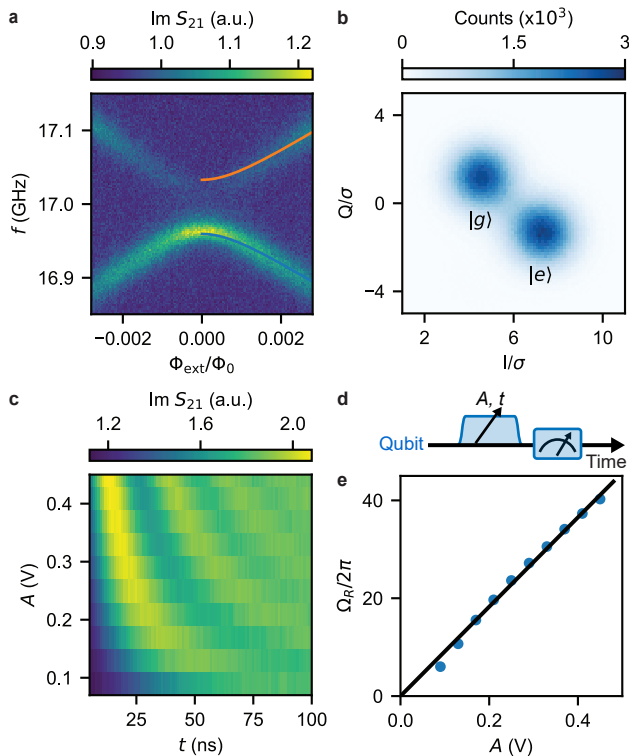


FIG. 2. **Qubit readout and control.** (a) Two tone spectroscopy near zero flux. The fit to the  $|g\rangle$ - $|e\rangle$  transition (blue line) and  $|g\rangle$ - $|f\rangle$  transition (orange line) is shown on the right half of the data. (b) Histogram of single-shot qubit readout. The qubit is populated to both the ground and excited state via a  $X_{\pi/2}$  pulse prior to measurement. We readout the qubit at the resonator frequency corresponding to qubit being in the  $|g\rangle$  state. (c) Rabi oscillations of the qubit versus a square pulse with room temperature drive amplitude  $A$  and length  $t$ . (d) Pulse sequence for the Rabi experiment shown in (c). (e) Rabi frequency as a function of  $A$ . We extract the Rabi frequencies from (c). The black line is a linear fit of the Rabi frequency versus drive amplitude.

described by Eq. 1 (solid lines in Fig. 2(a)) and observe good agreement between the data and theory. From the fit, we find  $E_L = 34.4$  GHz,  $E_{s,1} = 1.03$  GHz, and  $E_{s,2} = 0.05$  GHz. Though small, we find that the  $E_{s,2}$  term must be included in order to properly reproduce the spectroscopy data at zero flux (see Supplementary Information for additional discussion). As an additional check that the qubit is behaving as predicted, we note that this Hamiltonian enforces a parity selection rule at exactly zero flux for transitions between the  $|g\rangle$  and  $|f\rangle$  state, which we observe as a decrease in the visibility of that transition.

We also demonstrate our ability to perform single-shot readout, which is essential in implementing future quantum algorithms and quantum error correction schemes. We drove the qubit at the  $|g\rangle$ - $|e\rangle$  frequency to populate the qubit in both the ground and excited states, and measured the resonator response. We performed this measurement  $2 \times 10^6$  times and constructed a histogram of

the resulting data, which is presented in Fig. 2(b). We observe clear separation between the  $|g\rangle$  and  $|e\rangle$  resonator responses with an assignment fidelity of 96% [31].

We next demonstrate qubit control by driving Rabi oscillations between the ground state and the excited state. We applied a drive with amplitude,  $A$ , and varied the duration,  $t$ , before measuring the state of the qubit via a readout pulse as described by the sequence shown in Fig. 2(d). Figure 2(c) shows oscillations in the qubit state as a function of  $A$  and  $t$ . The extracted Rabi frequency for each pulse amplitude is plotted in Fig. 2(e). The measured Rabi frequency depends linearly on the amplitude, which we expect for the behavior of a driven qubit. We note that despite the proximity of the  $|g\rangle - |f\rangle$  transition to the  $|g\rangle - |e\rangle$  transition, we do not observe any spurious oscillations in Fig. 2(c). This further indicates that our phase slip qubit is behaving as a well-controlled two-level system, and is not leaking to the  $|f\rangle$  state.

We conducted time-domain measurements to characterize the qubit lifetime and coherence at the zero-flux sweet spot. We used standard measurement protocols to measure the relaxation time  $T_1$ , the Ramsey coherence time  $T_{2R}$ , and the single Hahn-echo coherence time  $T_{2E}$  (Fig. 3(a-c)). The observed  $T_1$  improves upon previously-measured relaxation times in phase slip qubits at  $\Phi_{\text{ext}} = 0.5\Phi_0$  by a factor of  $10^3$ . The  $T_{2R}$  is significantly smaller than  $T_1$ , however, which indicates strong qubit dephasing. The coherence time only partly improves with an echo pulse, indicating that the qubit may be suffering from high-frequency noise. The echo may also have resulted in limited improvement because our  $X_\pi$  pulse was imperfect. Due to limitations in drive power from our room-temperature electronics, the width of our applied pulses for these measurements was 9 ns, which is slightly more than half the measured  $T_{2R}$  time. Master equation simulations of our driven qubit suggest that our  $X_\pi$  and  $X_{\pi/2}$  pulses do not bring our qubit completely to  $|e\rangle$  and  $\frac{1}{\sqrt{2}}(|g\rangle + |e\rangle)$ , respectively (See Supplementary Information for more details).

Next, we investigate the flux and time dependence of  $T_1$  to identify the loss mechanisms affecting our phase slip qubit (Fig. 3(d)). The relaxation time demonstrates well-defined flux dependence around zero flux, but fluctuates significantly as the flux is moved away from zero flux as shown in the inset of Fig. 3(d). Near zero flux, we can model the flux dependence of the relaxation due to inductive loss [32] and find an inductive quality factor,  $Q_{\text{ind}} = 4.2 \times 10^4$ . The measured  $T_1$  deviates significantly from the fit as we sweep away from zero  $\Phi_0$ . From qubit spectroscopy in these regions, we suspect that the qubit may be coupling to multiple two-level systems (TLS), which would unpredictably degrade the relaxation time and contribute to this deviation (Supplementary Information). We have also measured  $T_1$  over multiple days at zero flux and observed fluctuations from  $T_1 = 40 - 70 \mu\text{s}$  (shown in the multiple data points at zero flux in Fig. 3(d)). We conjecture that this variability could also be due to spurious TLS coupling to the qubit,

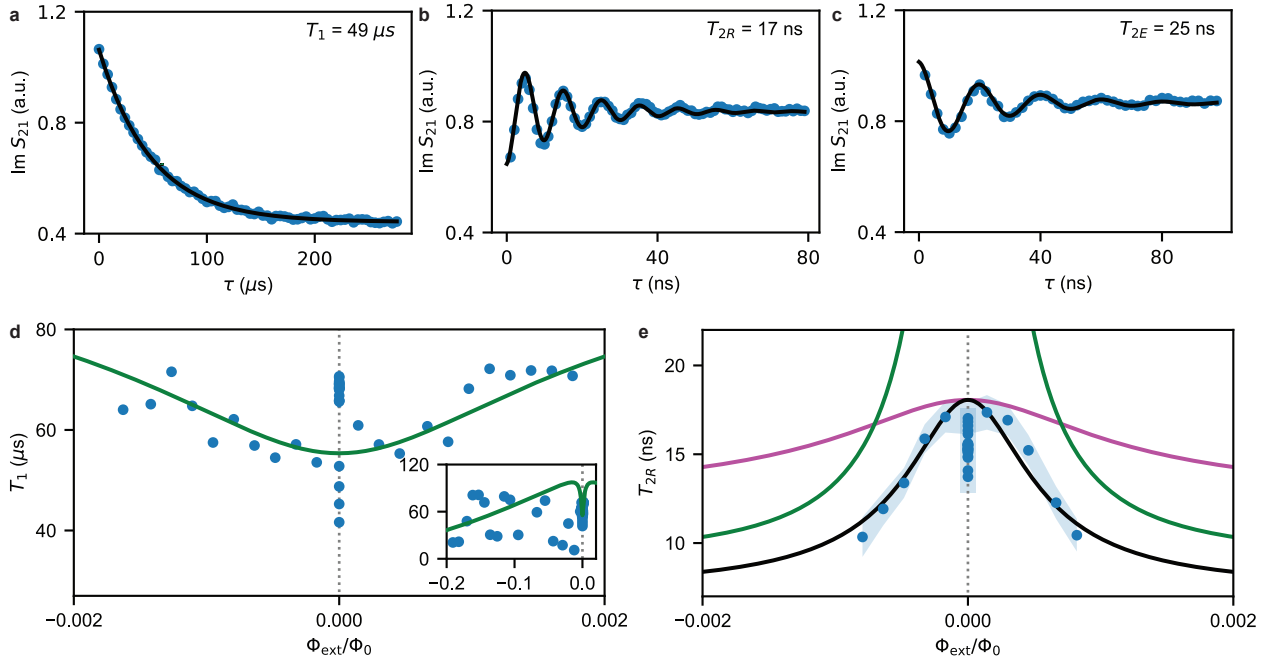


FIG. 3. **Qubit relaxation and coherence.** (a-c) Time domain measurements taken at zero flux measuring (a) the relaxation time  $T_1$ , (b) the Ramsey coherence time  $T_{2R}$ , and (c) the coherence time with the application of a single echo pulse  $T_{2E}$ . The duration of the  $X_\pi$  and  $X_{\pi/2}$  pulses used in the measurements was 9 ns. (d) Relaxation time  $T_1$  versus flux. The expected flux dependence of  $T_1$  due to inductive loss with  $Q_{\text{ind}} = 4.2 \times 10^4$  is plotted in green. The inset shows that  $T_1$  deviates from the inductive loss fit away from zero flux. The gray dotted line is a guide for the eye for zero flux. The range of variations of  $T_1$  in time is shown by the data points at zero flux. (e) Ramsey coherence time  $T_{2R}$  versus flux. The shaded region indicates the error from fitting the  $T_{2R}$  data. The green line shows the expected flux dependence of  $T_{2R}$  due to first-order flux noise dephasing with noise amplitude,  $A_\Phi = 1.2 \times 10^{-4} \Phi_0 / \sqrt{\text{Hz}}$ . The pink line is the limit set by Aharonov-Casher dephasing for variation in  $E_{s,1}$  with noise amplitude,  $A_{AC} = 0.037 E_{s,1} / \sqrt{\text{Hz}}$ . The black line shows the expected limit from the quadrature sum of both models. Similar to (d), the gray line is a guide for zero flux and the range of variations of  $T_{2R}$  in time is shown by the data points at zero flux. Note that at zero flux, only the point with the highest  $T_{2R}$  was included in the fit.

with the TLS landscape changing over time [33].

Next we performed  $T_{2R}$  measurements versus flux near zero flux to investigate the dephasing mechanisms of the qubit (Fig. 3(e)). We fit the data using two models: flux noise [34, 35] and Aharonov-Casher (AC) noise [36, 37], depicted by the green and pink lines in Fig. 3(e), respectively. The flux noise amplitude from the fit is  $A_\Phi = 1.2 \times 10^{-4} \Phi_0 / \sqrt{\text{Hz}}$ , which is  $\sim 2$  orders of magnitude larger than current state-of-the-art Josephson junction-based flux qubits [38]. Impurities introduced during device fabrication may be responsible for this increased flux noise [29].

Since the qubit is first-order insensitive to flux noise at zero flux, we introduce an additional dephasing mechanism due to Aharonov-Casher noise, which causes variations in  $E_{s,1}$  and  $E_{s,2}$ . This noise arises from multiple flux quanta with different phases coherently interfering with one another as they tunnel through the narrow constriction. The phase accumulated is dependent on the distribution of charges along the wire, which can vary in time [36, 37]. We obtain an AC noise amplitude,  $A_{AC}$ , of  $0.037 E_{s,1} / \sqrt{\text{Hz}}$  for variations in  $E_{s,1}$  assuming a simple

phenomenological model including the dependence of the Hamiltonian on changes to  $E_{s,1}$  at different flux points (See Supplementary Information for more details). We hypothesize that reducing the length of the PSJ to be smaller than the coherence length could decrease the dephasing due to AC noise. We include the effect of both noise mechanisms using the quadrature sum of their effects to find the total expected coherence time [37], which is shown by the black line in Fig. 3(e). We also monitored  $T_{2R}$  at zero flux over several days and observe small variations from  $T_{2R} = 14 - 17 \text{ ns}$ , as illustrated by the points on the gray dotted line in Fig. 3(e).

Finally, we investigate the benefits of the higher qubit frequency and larger gap of TiN in operating the phase slip qubit at higher temperatures. Figure 4(a-b) shows the measured relaxation time and coherence time of the qubit up to 385 mK. We observe that  $T_1$  remains above  $20 \mu\text{s}$  for temperatures up to 300 mK while  $T_{2R}$  remains essentially constant with temperature. The relaxation time shows a slow degradation up to 240 mK, after which  $T_1$  decreases significantly. Previous measurements of aluminum-based superconducting qubits have

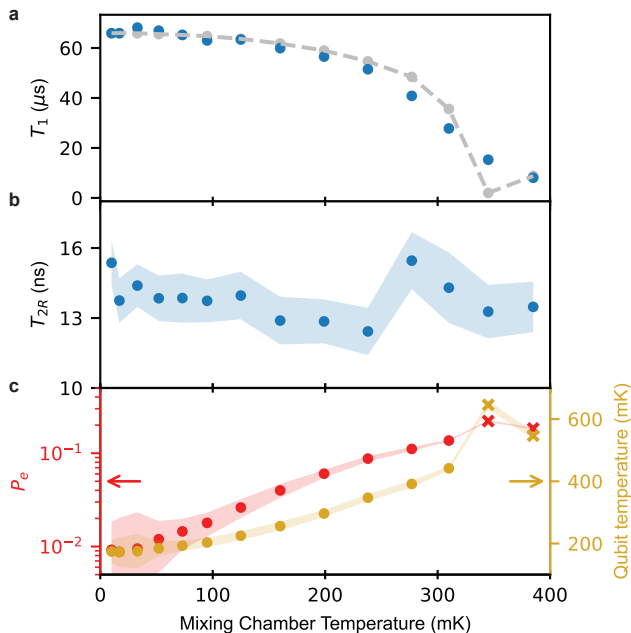


FIG. 4. **Operation of the qubit at elevated temperatures.** (a) Temperature dependence of qubit lifetime. The blue points are the measured  $T_1$  values. The gray points with dashed lines represent the expected  $T_1$  degradation due to decreasing  $Q_{\text{ind}}$  from the rise in the quasiparticle population as the qubit temperature increases. We use the measured qubit temperature as input to our model. (b) Temperature dependence of qubit coherence time. The shaded region is the error from the  $T_{2R}$  fit.  $T_{2R}$  does not show significant variation with temperature. (c) Excited state probability,  $P_e$  (left) and qubit temperature (right) as a function of mixing chamber temperature. The shaded regions represent the uncertainty from the qubit histogram fit. The crosses represent data which was taken with a different readout parameter compared to the circles, which was chosen due to the reduction in  $T_1$  at higher temperatures.

also observed a significant decrease in  $T_1$  at temperatures around 150 mK, which was attributed to an increase in quasiparticle loss [39–41].

The decreased  $T_1$  is surprising since the measured transition temperature of our TiN film is 2.9 K. We additionally measured the qubit excited-state population as a function of temperature to better understand the temperature dependence of the relaxation time as shown in Fig. 4(c). The measured probability is converted to qubit temperature using the Boltzmann distribution (right axis in Fig. 4(c)). The qubit temperature appears to be consistently greater than the mixing chamber temperature by  $>100$  mK. Using the measured qubit temperature, we model the reduction in lifetime as inductive loss, with  $Q_{\text{ind}}$  changing as a function of qubit temperature to reflect an increasing quasiparticle density as shown by the gray points with dashed lines in Fig. 4(a) (See Supplementary Information). We find reasonable agreement of the measured relaxation times to this model.

We have demonstrated all essential single-qubit func-

tions in a phase slip qubit operated at zero flux fabricated from a single layer of TiN. Our results show that the PSJ is a viable alternative source of nonlinearity that can be used in coherent quantum devices. Having multiple superconducting sources of nonlinearity significantly expands the possible quantum coherent devices that can be built. First, the PSJ acts as a nonlinear capacitor rather than a nonlinear inductor. A nonlinear capacitance allows for the creation of novel oscillators with photon-dependent non-linearities [7] that can be used for sensitive detection and signal amplification. Additionally, a nonlinear capacitor formed from a PSJ in parallel with a nonlinear inductor formed from a Josephson junction has the possibility of realizing quantum states that are protected from external noise [21]. Finally, we used a single TiN film to build our entire qubit-resonator device. Titanium nitride has been demonstrated to have higher quality factors than evaporated aluminum [25]. Our demonstrated PSJ qubit is thus a first step toward qubits with longer possible relaxation times than current AlOx-junction based superconducting qubits. Achieving longer qubit coherence times will be necessary for the phase slip qubit to become a competitive platform for quantum information processing. While our qubit has relaxation times comparable to standard JJ-based superconducting qubits, the coherence times of the qubit are very short. Improved cleaning methods in the device processing or changes in the geometry to reduce sensitivity to fluctuating charges on the PSJ will further elucidate these decoherence mechanisms.

Our phase slip qubit design operated at zero flux presents a platform for building high frequency qubits that can operate at high temperatures. Building superconducting qubits that can operate at high temperatures has become increasingly important as superconducting quantum processors run into limits imposed by cooling capabilities of current technologies. While we observed that the qubit relaxation time started to degrade significantly at temperatures below the superconducting transition temperature, our demonstrated qubit operation above 100 mK already significantly reduces the technological requirements needed to cool superconducting qubits beyond what can be achieved by aluminum-based superconducting qubits. The observed poor thermalization of the qubit suggests multiple paths forward for further increasing the qubit operating temperature. It may be possible that the qubit is coupled to a different bath compared with current superconducting qubits due to its high frequency, which would require additional filtering compared to standard devices. The very thin superconducting TiN film may also have large enough disorder to prolong thermalization times; measurements of qubits made using superconducting films with different levels of disorder will be useful in understanding this mechanism. Usage of superconducting films with even higher transition temperatures than TiN may present a path to superconducting qubits operating above 4 K.

## METHODS

### A. Device fabrication

We fabricated the sample from a 5 nm thick TiN film on a 720  $\mu\text{m}$  thick silicon substrate. Smaller features such as the resonator and the qubit were fabricated using electron-beam lithography (Elionix ELS-G150) with ZEP 520A resist. We used photolithography (Heidelberg MLA 150) with AZ1518 resist to pattern larger features such as the ground plane and transmission line. The sample was etched after each patterning step using an Oxford Mixed ICP-RIE system with a chemistry of  $\text{Cl}_2$ ,  $\text{BCl}_3$ , and Ar. To clean the sample, we used an  $\text{O}_2$  descum process, followed by rinsing in N-Methylpyrrolidone (NMP). Prior to wirebonding to a printed circuit board, the sample was rinsed in buffered oxide etchant (BOE) to remove surface oxides.

### B. Experimental Setup

The sample was enclosed in a Copper sample holder and cooled to 10 mK in a dilution refrigerator (Oxford Instruments, Triton 500). A coil was mounted to the sample holder and a DC current source (Yokogawa, GS200) was used to apply magnetic field to the sample. The readout and qubit pulses were formed by mixing local oscillator (LO) tones from signal generators with IQ tones from an integrated FPGA system (Quantum Machines, OPX+). The input signal was thermalized via attenuators at different temperature plates before reaching the mixing chamber. At the mixing chamber plate, the input was sent through an Eccosorb filter to filter out high-frequency noise before entering the transmission line.

The output from the transmission line was routed through another Eccosorb filter followed by a traveling wave parametric amplifier (TWPA). The output sig-

nal was then amplified again at the 4K plate via a high-electron-mobility transistor (HEMT) amplifier (Low Noise Factory, LNF-LNC4\_16B) and at room temperature via a low noise amplifier (LNF-LNR4\_14B\_SV). The signal was demodulated and further amplified before being sent to the FPGA for processing.

### C. Simulations

Prior to measurements, we estimated the resonator frequency and coupling quality factor using electromagnetic field simulation (Ansys HFSS). To solve the Hamiltonian and estimate qubit frequency, we employed numerical diagonalization in QuTip [42]. We also used QuTip to fit the qubit spectroscopy and perform master equation pulse-level simulations (See Supplementary Information).

### ACKNOWLEDGMENTS

We thank Matthias Steffen, Benjamin Wymore, Oliver Dial, Aayam Bista, Xi Cao, Jared Gibson, Jinwoong Philip Kim, Michael Mollenhauer, Ke Nie, and Randy Owen for useful discussions. The TiN film and traveling-wave parametric amplifier used in this experiment were provided by IBM. This research was carried out in part in the Materials Research Lab Central Facilities and the Holonyak Micro and Nanotechnology Lab, University of Illinois. This research is funded through the IBM-Illinois Discovery Accelerator Institute.

### AUTHOR CONTRIBUTIONS

C.P. designed and measured the devices. K.C. and C.P. fabricated the devices. C.P. performed the data analysis with input from B.v.H. and A.K. C.P. and A.K. wrote the manuscript, with feedback from all authors. A.K. conceived and supervised the experiment.

- 
- [1] B. Yurke, L. R. Corruccini, P. G. Kaminsky, L. W. Rupp, A. D. Smith, A. H. Silver, R. W. Simon, and E. A. Whitaker, Observation of parametric amplification and deamplification in a Josephson parametric amplifier, *Physical Review A* **39**, 2519 (1989).
  - [2] C. Macklin, K. O'Brien, D. Hover, M. E. Schwartz, V. Bolkhovskiy, X. Zhang, W. D. Oliver, and I. Siddiqi, A near-quantum-limited Josephson traveling-wave parametric amplifier, *Science* **350**, 307 (2015).
  - [3] E. D. Walsh, W. Jung, G.-H. Lee, D. K. Efetov, B.-I. Wu, K.-F. Huang, T. A. Ohki, T. Taniguchi, K. Watanabe, P. Kim, D. Englund, and K. C. Fong, Josephson junction infrared single-photon detector, *Science* **372**, 409 (2021).
  - [4] M. Kjaergaard, M. E. Schwartz, J. Braumüller, P. Krantz, J. I.-J. Wang, S. Gustavsson, and W. D. Oliver, Superconducting Qubits: Current State of Play, *Annual Review of Condensed Matter Physics* **11**, 369 (2020).
  - [5] P. Krantz, M. Kjaergaard, F. Yan, T. P. Orlando, S. Gustavsson, and W. D. Oliver, A quantum engineer's guide to superconducting qubits, *Applied Physics Reviews* **6**, 021318 (2019).
  - [6] J. E. Mooij and C. J. P. M. Harmans, Phase-slip flux qubits, *New Journal of Physics* **7**, 219 (2005).
  - [7] A. M. Hriscu and Y. V. Nazarov, Model of a Proposed Superconducting Phase Slip Oscillator: A Method for Obtaining Few-Photon Nonlinearities, *Physical Review Letters* **106**, 077004 (2011).
  - [8] J. E. Mooij and Y. V. Nazarov, Superconducting nanowires as quantum phase-slip junctions, *Nature Physics* **2**, 169 (2006).
  - [9] O. V. Astafiev, L. B. Ioffe, S. Kafanov, Y. A. Pashkin, K. Y. Arutyunov, D. Shahar, O. Cohen, and J. S. Tsai, Coherent quantum phase slip, *Nature* **484**, 355 (2012).

- [10] J. Potter, J. Fenton, and P. Warburton, Controllable Tunneling of Single Flux Quanta Mediated by Quantum Phase Slip in Disordered Superconducting Loops, *Physical Review Applied* **19**, 024002 (2023).
- [11] J. T. Peltonen, Z. H. Peng, Y. P. Korneeva, B. M. Voronov, A. A. Korneev, A. V. Semenov, G. N. Gol'tsman, J. S. Tsai, and O. V. Astafiev, Coherent dynamics and decoherence in a superconducting weak link, *Physical Review B* **94**, 180508 (2016).
- [12] T. Hönlgl-Decrinis, I. Antonov, R. Shaikhaidarov, K. H. Kim, V. N. Antonov, and O. V. Astafiev, Capacitive coupling of coherent quantum phase slip qubits to a resonator, *New Journal of Physics* **25**, 113020 (2023).
- [13] J. T. Peltonen, O. V. Astafiev, Y. P. Korneeva, B. M. Voronov, A. A. Korneev, I. M. Charaev, A. V. Semenov, G. N. Golt'sman, L. B. Ioffe, T. M. Klapwijk, and J. S. Tsai, Coherent flux tunneling through NbN nanowires, *Physical Review B* **88**, 220506 (2013).
- [14] A. Belkin, M. Belkin, V. Vakaryuk, S. Khlebnikov, and A. Bezryadin, Formation of Quantum Phase Slip Pairs in Superconducting Nanowires, *Physical Review X* **5**, 021023 (2015).
- [15] S. E. De Graaf, S. T. Skacel, T. Hönlgl-Decrinis, R. Shaikhaidarov, H. Rotzinger, S. Linzen, M. Ziegler, U. Hübner, H.-G. Meyer, V. Antonov, E. Il'ichev, A. V. Ustinov, A. Y. Tzalenchuk, and O. V. Astafiev, Charge quantum interference device, *Nature Physics* **14**, 590 (2018).
- [16] R. S. Shaikhaidarov, K. H. Kim, J. W. Dunstan, I. V. Antonov, S. Linzen, M. Ziegler, D. S. Golubev, V. N. Antonov, E. V. Il'ichev, and O. V. Astafiev, Quantized current steps due to the a.c. coherent quantum phase-slip effect, *Nature* **608**, 45 (2022).
- [17] V. E. Manucharyan, J. Koch, L. I. Glazman, and M. H. Devoret, Fluxonium: Single Cooper-Pair Circuit Free of Charge Offsets, *Science* **326**, 113 (2009).
- [18] K. Kalashnikov, W. T. Hsieh, W. Zhang, W.-S. Lu, P. Kamenov, A. Di Paolo, A. Blais, M. E. Gershenson, and M. Bell, Bifluxon: Fluxon-Parity-Protected Superconducting Qubit, *PRX Quantum* **1**, 010307 (2020).
- [19] P. Brooks, A. Kitaev, and J. Preskill, Protected gates for superconducting qubits, *Physical Review A* **87**, 052306 (2013).
- [20] A. Gyenis, P. S. Mundada, A. Di Paolo, T. M. Hazard, X. You, D. I. Schuster, J. Koch, A. Blais, and A. A. Houck, Experimental Realization of a Protected Superconducting Circuit Derived from the  $0 - \pi$  Qubit, *PRX Quantum* **2**, 010339 (2021).
- [21] D. T. Le, A. Grimsmo, C. Müller, and T. M. Stace, Doubly nonlinear superconducting qubit, *Physical Review A* **100**, 062321 (2019).
- [22] W. Ardati, S. Léger, S. Kumar, V. N. Suresh, D. Nicolas, C. Mori, F. D'Esposito, T. Vakhitel, O. Buisson, Q. Ficheux, and N. Roch, Using Bifluxon Tunneling to Protect the Fluxonium Qubit, *Physical Review X* **14**, 041014 (2024).
- [23] R. A. Mencia, W.-J. Lin, H. Cho, M. G. Vavilov, and V. E. Manucharyan, Integer Fluxonium Qubit, *PRX Quantum* **5**, 040318 (2024).
- [24] J. E. Mooij, T. P. Orlando, L. Levitov, L. Tian, C. H. Van Der Wal, and S. Lloyd, Josephson Persistent-Current Qubit, *Science* **285**, 1036 (1999).
- [25] K. R. Amin, C. Ladner, G. Jourdan, S. Hentz, N. Roch, and J. Renard, Loss mechanisms in TiN high impedance superconducting microwave circuits, *Applied Physics Letters* **120**, 164001 (2022).
- [26] C. Joshi, W. Chen, H. G. LeDuc, P. K. Day, and M. Mirhosseini, Strong Kinetic-Inductance Kerr Nonlinearity with Titanium Nitride Nanowires, *Physical Review Applied* **18**, 064088 (2022).
- [27] A. Shearrow, G. Koolstra, S. J. Whiteley, N. Earnest, P. S. Barry, F. J. Heremans, D. D. Awschalom, E. Shirokoff, and D. I. Schuster, Atomic layer deposition of titanium nitride for quantum circuits, *Applied Physics Letters* **113**, 212601 (2018).
- [28] M. R. Vissers, J. Gao, D. S. Wisbey, D. A. Hite, C. C. Tsuei, A. D. Corcoles, M. Steffen, and D. P. Pappas, Low loss superconducting titanium nitride coplanar waveguide resonators, *Applied Physics Letters* **97**, 232509 (2010).
- [29] N. Saveskul, N. Titova, E. Baeva, A. Semenov, A. Lubenchenko, S. Saha, H. Reddy, S. Bogdanov, E. Marinero, V. Shalaev, A. Boltasseva, V. Khrapai, A. Kardakova, and G. Goltsman, Superconductivity Behavior in Epitaxial Ti N Films Points to Surface Magnetic Disorder, *Physical Review Applied* **12**, 054001 (2019).
- [30] A. Blais, J. Gambetta, A. Wallraff, D. I. Schuster, S. M. Girvin, M. H. Devoret, and R. J. Schoelkopf, Quantum-information processing with circuit quantum electrodynamics, *Physical Review A* **75**, 032329 (2007).
- [31] J. Gambetta, W. A. Braff, A. Wallraff, S. M. Girvin, and R. J. Schoelkopf, Protocols for optimal readout of qubits using a continuous quantum nondemolition measurement, *Physical Review A* **76**, 012325 (2007).
- [32] W. C. Smith, A. Kou, X. Xiao, U. Vool, and M. H. Devoret, Superconducting circuit protected by two-Cooper-pair tunneling, *npj Quantum Information* **6**, 1 (2020).
- [33] T. Thorbeck, A. Eddins, I. Lauer, D. T. McClure, and M. Carroll, Two-Level-System Dynamics in a Superconducting Qubit Due to Background Ionizing Radiation, *PRX Quantum* **4**, 020356 (2023).
- [34] R. H. Koch, J. Clarke, W. M. Goubau, J. M. Martinis, C. M. Pegrum, and D. J. Van Harlingen, Flicker (1/f) noise in tunnel junction dc SQUIDS, *Journal of Low Temperature Physics* **51**, 207 (1983).
- [35] G. Ithier, E. Collin, P. Joyez, P. J. Meeson, D. Vion, D. Esteve, F. Chiarello, A. Shnirman, Y. Makhlin, J. Schrieffer, and G. Schön, Decoherence in a superconducting quantum bit circuit, *Physical Review B* **72**, 134519 (2005).
- [36] V. E. Manucharyan, N. A. Masluk, A. Kamal, J. Koch, L. I. Glazman, and M. H. Devoret, Evidence for coherent quantum phase slips across a Josephson junction array, *Physical Review B* **85**, 024521 (2012).
- [37] M. T. Randeria, T. M. Hazard, A. Di Paolo, K. Azar, M. Hays, L. Ding, J. An, M. Gingras, B. M. Niedzielski, H. Stickler, J. A. Grover, J. L. Yoder, M. E. Schwartz, W. D. Oliver, and K. Serniak, Dephasing in Fluxonium Qubits from Coherent Quantum Phase Slips, *PRX Quantum* **5**, 030341 (2024).
- [38] L. B. Nguyen, Y.-H. Lin, A. Somoroff, R. Mencia, N. Grabon, and V. E. Manucharyan, High-Coherence Fluxonium Qubit, *Physical Review X* **9**, 041041 (2019).
- [39] H. Paik, D. I. Schuster, L. S. Bishop, G. Kirchmair, G. Catelani, A. P. Sears, B. R. Johnson, M. J. Reagor, L. Frunzio, L. I. Glazman, S. M. Girvin, M. H. Devoret, and R. J. Schoelkopf, Observation of High Coherence in Josephson Junction Qubits Measured in a Three-

- Dimensional Circuit QED Architecture, *Physical Review Letters* **107**, 240501 (2011).
- [40] K. Serniak, M. Hays, G. De Lange, S. Diamond, S. Shankar, L. Burkhardt, L. Frunzio, M. Houzet, and M. Devoret, Hot Nonequilibrium Quasiparticles in Transmon Qubits, *Physical Review Letters* **121**, 157701 (2018).
- [41] J. M. Martinis, M. Ansmann, and J. Aumentado, Energy Decay in Superconducting Josephson-Junction Qubits from Nonequilibrium Quasiparticle Excitations, *Physical Review Letters* **103**, 097002 (2009).
- [42] J. Johansson, P. Nation, and F. Nori, QuTiP 2: A Python framework for the dynamics of open quantum systems, *Computer Physics Communications* **184**, 1234 (2013).

# Supplementary Information for Operation of a high-frequency, superconducting phase-slip qubit

Cheeranjeev Purmessur,<sup>1</sup> Kaicheung Chow,<sup>2</sup> Bernard van Heck,<sup>3</sup> and Angela Kou<sup>1,2,4</sup>

<sup>1</sup>*Department of Physics, University of Illinois Urbana-Champaign, Urbana, IL 61801*

<sup>2</sup>*Holonyak Micro & Nanotechnology Lab, University of Illinois Urbana-Champaign, Urbana, IL 61801*

<sup>3</sup>*Dipartimento di Fisica, Sapienza Università di Roma, 00185 Roma, IT*

<sup>4</sup>*Materials Research Laboratory, University of Illinois at Urbana-Champaign, Urbana, IL 61801*

(Dated: February 12, 2025)

## I. FULL DEVICE

The full device including both the lumped-element resonator and the qubit is shown in Fig. S1. The lumped-element resonator consists of two capacitor pads and an inductance formed from a narrow strip (width 570 nm) of TiN. The ground plane (not shown in the figure) is located 15  $\mu\text{m}$  from the top and bottom edges of pads and 125  $\mu\text{m}$  from the left and right edges. The ground plane contains holes to trap magnetic vortices present around the device. Input readout and qubit pulses were coupled to the device via a transmission line. From resonator spectroscopy at zero flux, we obtain a coupling quality factor,  $Q_c = 1.8 \times 10^3$  and an internal quality factor,  $Q_i = 4.9 \times 10^5$  when driving with a single photon.

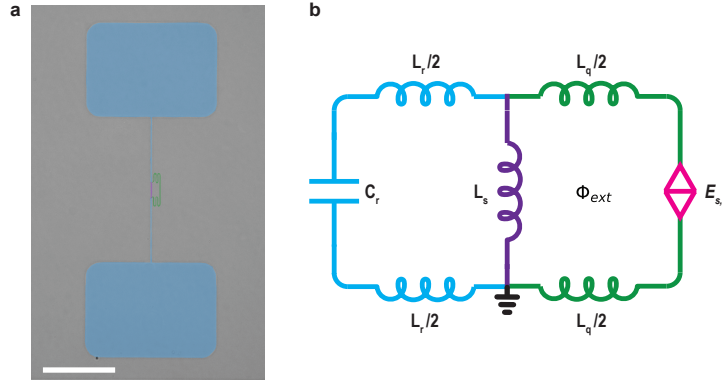


FIG. S1. **Full device** (a) False-colored SEM image of a lithographically similar device to device A showing the resonator and qubit. The scale bar corresponds to 50  $\mu\text{m}$ . (b) Circuit schematic of the full device. In (a) and (b), the qubit (green) is inductively coupled to the resonator (blue) via a shared inductance (purple). The PSJ is shown in pink.

The full Hamiltonian of the qubit coupled to the resonator is given by

$$H_{\text{sys}} = H_q + H_r + H_c \quad (1)$$

where  $H_c$  is the interaction Hamiltonian, representing the coupling between the resonator and the qubit. Below we write the resonator  $H_r$ , qubit  $H_q$ , and interaction Hamiltonians (with  $\hbar = 1$ ).

$$H_q = \frac{E_L}{2} \sum_m \left[ \left( m - \frac{\Phi_{\text{ext}}}{\Phi_0} \right)^2 |m\rangle \langle m| \right] - \frac{E_{s,1}}{2} \sum_m (|m\rangle \langle m+1| + |m+1\rangle \langle m|) + \frac{E_{s,2}}{2} \sum_m (|m\rangle \langle m+2| + |m+2\rangle \langle m|) \quad (2)$$

$$H_r = 4E_{C_r} \hat{n}_r^2 + \frac{1}{2} E_{L_r} \hat{\phi}_r^2 \quad (3)$$

$$H_c = g \sum_m \left( m - \frac{\Phi_{\text{ext}}}{\Phi_0} \right) |m\rangle \langle m| \times \frac{\hat{\phi}_r}{\sqrt{\zeta}/2} \quad (4)$$

where  $\hat{n}_r$  and  $\hat{\phi}_r$  are the Cooper pair number and phase operators of the resonator with  $\hat{n}_r = (1/\sqrt{2\zeta})i(a - a^\dagger)$  and  $\hat{\phi}_r = \sqrt{\zeta}/2(a + a^\dagger)$ . Here,  $\zeta = \sqrt{8E_{Cr}/E_{Lr}}$  is defined as the resonator impedance and  $a$  and  $a^\dagger$  are the ladder operators.  $E_{Cr}$ ,  $E_{Lr}$ , and  $g$  are the charging energy, inductive energy, and coupling strength, respectively. To express  $E_{Cr}$ ,  $E_{Lr}$ ,  $g$ , and  $E_L$  in terms of  $L_r$ ,  $C_r$ ,  $L_s$ , and  $L_q$ , we applied Kirchhoff's laws and solved for the Hamiltonian of the circuit (Fig. S1 (b)). We define the following terms:

$$L'_T = L_q L_r + L_s L_r + L_s L_q \quad (5)$$

$$\frac{1}{L'_q} = \frac{1}{L'_T}(L_s + L_r) \quad (6)$$

$$\frac{1}{L'_r} = \frac{1}{L'_T}(L_s + L_q) \quad (7)$$

Here we refer to  $L'_q$  and  $L'_r$  as the effective qubit and resonator inductance, respectively. Then,

$$E_{Cr} = \frac{e^2}{2C_r}, \quad E_{Lr} = \left(\frac{\Phi_0}{2\pi}\right)^2 \frac{1}{L'_r}, \quad g = \frac{\Phi_0}{2\pi} \Phi_0 \frac{L_s}{L'_t} \sqrt{\frac{\zeta}{2}}, \quad E_L = \frac{\Phi_0^2}{L'_q} \quad (8)$$

## II. FULL QUBIT SPECTRUM AND RESONATOR SPECTRUM FIT

In Fig. S2, we show the resonator and qubit spectroscopy data for  $\Phi_{\text{ext}}/\Phi_0 \approx [-0.56, 0]$ . We fitted both sets of data to our system Hamiltonian and obtained  $f_r = 5.264$  GHz and  $g = 1.146$  GHz along with the  $E_L$ ,  $E_{s,1}$ , and  $E_{s,2}$  values mentioned in the main text. From the fitted  $E_L$  value, we estimate a kinetic inductance per square,  $L_k/\square = 380$  pH/ $\square$ . For the qubit spectroscopy fit, we used all the blue data points for the  $|g\rangle - |e\rangle$  transition and the orange data points for the  $|g\rangle - |f\rangle$  transition in Fig. S2(b). We calibrated the flux to applied current conversion using qubit measurements close to the sweet spots  $\Phi_{\text{ext}} = 0, 0.5\Phi_0$ , and measurements of the resonator frequency versus flux. In the region between  $\Phi_{\text{ext}} = -0.31\Phi_0$  and  $\Phi_{\text{ext}} = -0.01\Phi_0$ , we observe flux hysteresis as well as a large number of two-level systems (TLS) coupled to the qubit, which altered the flux dependence of the qubit spectrum. For the region between  $\Phi_{\text{ext}} = -0.31\Phi_0$  and  $\Phi_{\text{ext}} = -0.27\Phi_0$ , the resonator frequency has a strong flux dependence due to the dispersive shift induced by the qubit, which allowed us to independently identify the flux location of qubit spectroscopy points in the presence of flux jumps and coupled TLS modes. At points  $\Phi_{\text{ext}} = [-0.27, -0.01]\Phi_0$ , however, the resonator spectrum becomes flat versus flux, which made precise calibration of the flux difficult in this region. These data points are shown as color maps with our best estimate of the flux and are not included in the fit (Fig. S2(b)).

## III. INCLUSION OF THE $E_{s,2}$ TERM

In  $H_{\text{sys}}$ , the  $E_{s,1}$  term determines the  $|g\rangle$  to  $|e\rangle$  energy splitting at half flux. The  $E_{s,2}$  term does not contribute to this splitting because, at half flux, the states involved differ by only one fluxon. Our data at half flux thus fixes the value of  $E_{s,1}$ . Near zero flux, transitions from the ground state to the  $|e\rangle$  and  $|f\rangle$  states involve tunneling of two fluxons, which can be sequential or simultaneous. Thus it is possible that  $E_{s,2}$ , which describes simultaneous flux tunneling, contributes to the energy splitting. In Fig. S3, we fit the two tone spectroscopy near zero flux to (a)  $H_{\text{sys}}$  and (b)  $H_{\text{sys}}$  without the  $E_{s,2}$  term. The fitted parameters extracted for  $H_{\text{sys}}$  without  $E_{s,2}$  are  $E_L = 34.4$  GHz and  $E_{s,1} = 1.03$  GHz. Clearly in (b), if we exclude  $E_{s,2}$ , the fit underestimates the energy splitting between the  $|e\rangle$  and  $|f\rangle$  state. Therefore,  $E_{s,2}$  is necessary to describe the measured  $|e\rangle$  and  $|f\rangle$  energy splitting.

## IV. MASTER EQUATION SIMULATION

Given that our measurement pulse duration (9 ns) is not significantly shorter than the qubit coherence time, we suspect that our  $X_\pi$  and  $X_{\pi/2}$  measurement pulses are imperfect. They would therefore not bring the qubit completely to the  $|e\rangle$  or  $\frac{1}{2}(|g\rangle + |e\rangle)$  states during the time domain measurements. More specifically, for the qubit relaxation

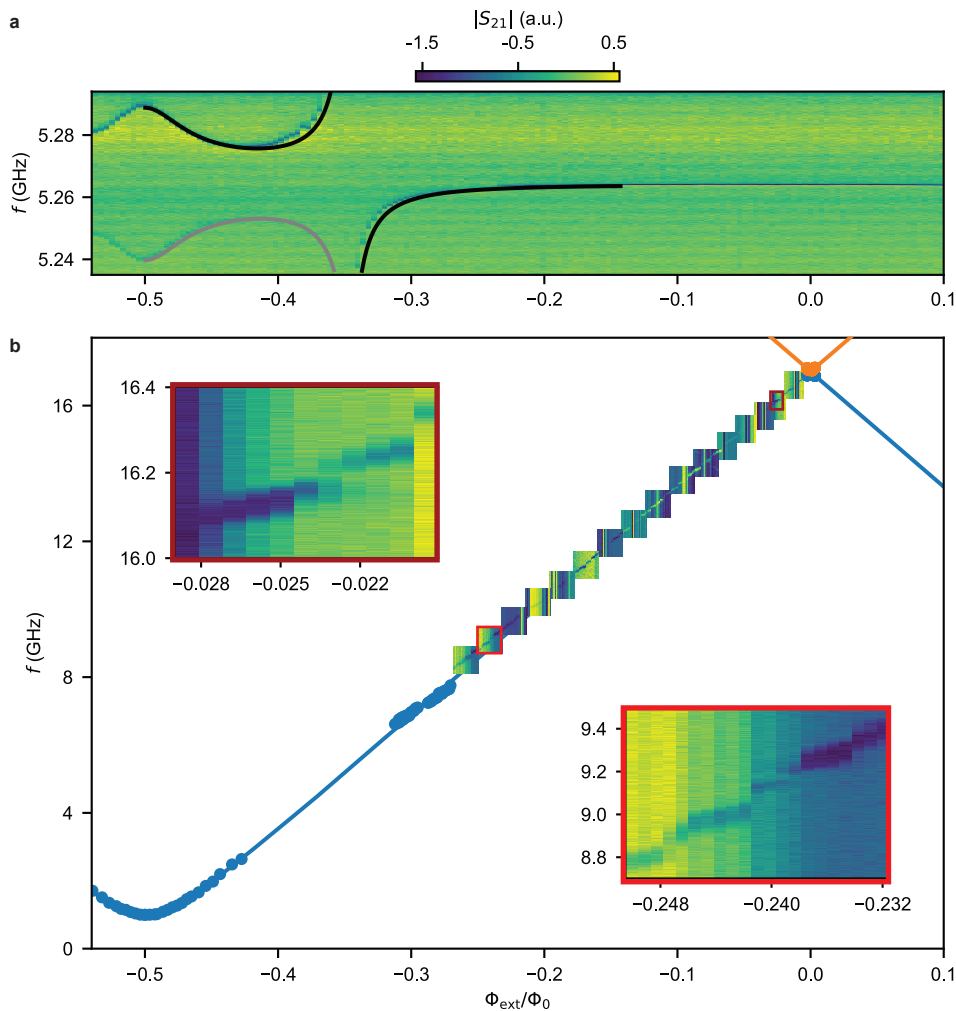


FIG. S2. **Resonator spectrum and full qubit spectrum** (a) Resonator spectroscopy fit and data. The black line denotes the  $|g, 0\rangle - |g, 1\rangle$  transition while the gray line denotes the  $|e, 0\rangle - |e, 1\rangle$  transition. From the fit,  $f_r = 5.264$  GHz and  $g = 1.146$  GHz. (b) Qubit spectroscopy fit and data. The blue and orange points are the  $|g\rangle - |e\rangle$  and  $|g\rangle - |f\rangle$  frequency points, respectively, that are used for fitting. The flux of these points have been calibrated using the resonator frequency points in those regions. The 2D color maps on the slope of the  $|g\rangle - |e\rangle$  shows the coupling of the qubit to multiple TLS's.

measurement, the qubit is most likely not 100% in the  $|e\rangle$  state to start with but rather in some mixture of  $|g\rangle$  and  $|e\rangle$ . We conduct a pulse-level master equation simulation in QuTip to quantify the imperfection of our  $X_\pi$  and  $X_{\pi/2}$  pulses [1]. In the simulation, we specify the relaxation and dephasing rates at zero flux in the collapse operators. The results of these simulations can be found in Fig. S4. We obtain a probability of being in the excited state,  $P_e = 0.88$  after applying a  $X_\pi$  pulse and  $P_e = 0.43$  after applying a  $X_{\pi/2}$  pulse.

## V. QUBIT LIFETIME VS FLUX ANALYSIS

We model the flux dependence of the relaxation time using the inductive loss model described in [2]. Employing Fermi's golden rule, we can relate the relaxation rate due to inductive loss to the matrix element of the flux across the superinductance,  $\langle e | \hat{\Phi} | g \rangle$ , and the power spectral density of the noise,  $S(\omega_{eg})$ .

$$\frac{1}{T_1} = \Gamma_1 = \frac{1}{\hbar^2} \left| \langle e | \hat{\Phi} | g \rangle \right|^2 [S(\omega_{eg}) + S(-\omega_{eg})] \quad (9)$$

In the expression above, the relaxation rate due to both emission and absorption is included. The sum of the noise spectral densities is given by

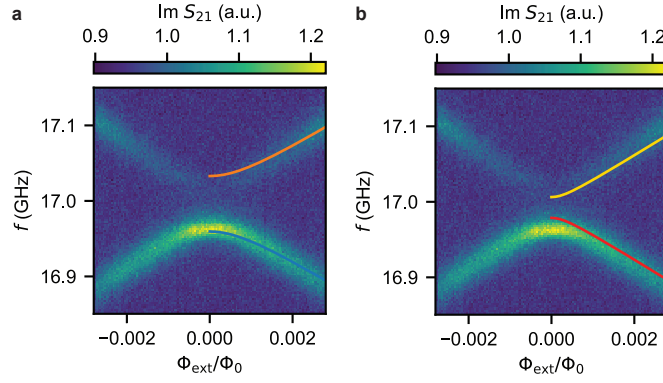


FIG. S3. **Fitting to  $H_{\text{sys}}$  with and without the  $E_{s,2}$  term** (a) Fit to  $H_{\text{sys}}$  including both the  $E_{s,1}$  and  $E_{s,2}$  terms. The blue line is the  $|g\rangle - |e\rangle$  fit and the orange line is  $|g\rangle - |f\rangle$  fit. (b) Fit to  $H_{\text{sys}}$  excluding the  $E_{s,2}$  term. The red line is the  $|g\rangle - |e\rangle$  fit and the yellow line is  $|g\rangle - |f\rangle$  fit.

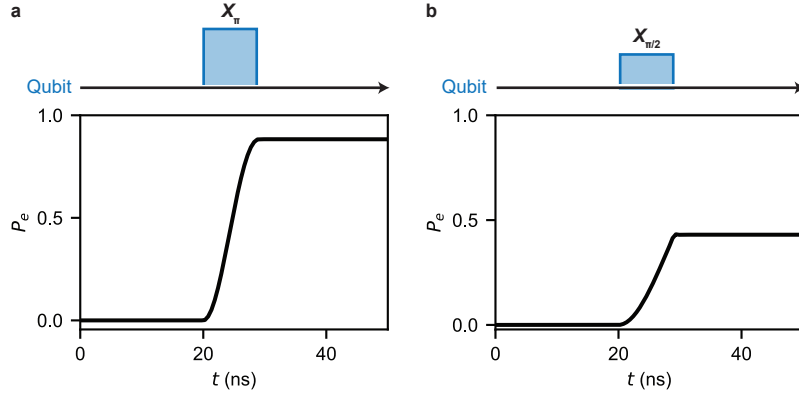


FIG. S4. **Pulse-level master equation simulation results** (a) and (b) show the probability of the qubit being in the  $|e\rangle$  state after applying a  $X_\pi$  and  $X_{\pi/2}$  pulse, respectively. The duration of the pulses is set to 9 ns, which is the pulse length used in our experiment.

$$S(\omega_{ge}) + S(-\omega_{ge}) = \frac{2\hbar}{LQ_{\text{ind}}} \coth \frac{\hbar|\omega_{ge}|}{2k_B T} \quad (10)$$

Here  $L$  is the effective qubit inductance,  $Q_{\text{ind}}$  is the inductive quality factor and  $T$  is the bath temperature. We assume that  $T = 174$  mK, which is the temperature of the qubit at the base mixing chamber temperature (See Fig. 4 of the main text). In Fig. S5 (a), we show the  $T_1$  data that was taken in the range  $\Phi_{\text{ext}}/\Phi_0 \approx [-0.56, 0]$ . We see a clear flux dependence for data around  $-0.5\Phi_0$ . The olive green line is the fit for the data in this region, where we obtain  $Q_{\text{ind}} = 6.6 \times 10^5$ . The darker green line is the expected  $T_1$  values when  $Q_{\text{ind}} = 4.2 \times 10^4$ . This line is also shown near zero flux in Fig. 3(d) of the main text. It appears that the  $Q_{\text{ind}}$  varies at different flux points (or qubit frequencies). Fig. S5 (b) shows the same  $T_1$  data and fit with the qubit frequency on the x-axis. The data in the range  $f \approx [4, 16.8]$  GHz (or  $\Phi_{\text{ext}}/\Phi_0 \approx [-0.4, -0.01]$ ) does not agree well with either fit. There are clear frequency regions where the  $T_1$  degrades before it improves again. We conjecture that the presence of multiple TLS could be causing the large variability in  $T_1$ . Examples of TLS in the particular frequency (or flux) range is shown in the inset of Fig. S2(b). We do not see  $T_1$  variability for  $f < 4$  GHz. Further investigation is needed to determine the TLS spectral density of the TiN material. Note that the Purcell loss limit is significantly higher than our measured relaxation times at  $-0.5\Phi_0$  or at  $0\Phi_0$  when setting the bath temperature to  $T = 174$  mK.

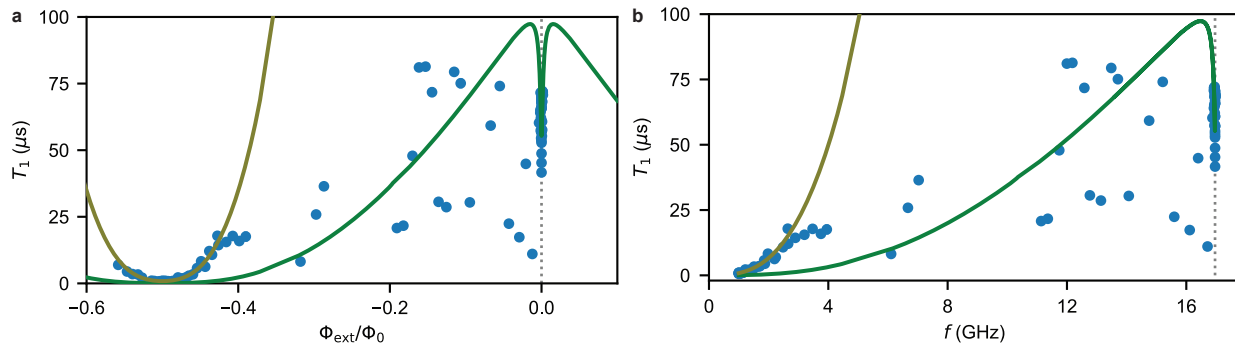


FIG. S5. **Full qubit lifetime data and fit** (a)  $T_1$  as a function of flux. (b)  $T_1$  as a function of qubit frequency. In (a) and (b), the expected  $T_1$  due to inductive loss with  $Q_{\text{ind}} = 6.6 \times 10^5$  is plotted in olive green and agrees well with the  $T_1$  data taken around  $-0.5\Phi_0$ . The darker green line is the fit around  $0\Phi_0$  with  $Q_{\text{ind}} = 4.2 \times 10^4$ . The data in the range  $\Phi_{\text{ext}}/\Phi_0 \approx [-0.4, -0.01]$  or  $f \approx [4, 16.8]$  GHz deviates significantly from the fits. We attribute this deviation to the presence of TLS residing at specific qubit frequencies.

## VI. QUBIT COHERENCE VS FLUX ANALYSIS

In Fig. 3(e) of the main text, we fit the  $T_{2R}$  vs flux using the quadrature sum of the dephasing rate from both the flux noise and Aharonov-Casher(AC) noise contributions since we assume that these noise contributions are independent and Gaussian distributed [3].

$$\frac{1}{T_{\varphi R}} = \Gamma_{\varphi R} = \sqrt{(\Gamma_{\varphi R}^{\Phi})^2 + (\Gamma_{\varphi R}^{\text{AC}})^2} \quad (11)$$

To obtain the  $T_{2R}$  vs flux fit (black line in Fig. 3(e) of the main text), we use

$$\frac{1}{T_{2R}} = \frac{1}{2T_1} + \frac{1}{T_{\varphi R}} \quad (12)$$

where  $T_{\varphi R}$  is obtained from Eq.11. We set  $T_1$  to the values obtained in the  $T_1$  vs flux fit near zero flux. However,  $T_{2R} \approx T_{\varphi R}$  since  $T_1 \gg T_{\varphi R}$ . Below, we go through the analysis for the dephasing rate from both the flux noise and the Aharonov-Casher noise.

### A. Dephasing from flux noise

The flux noise spectral density is generally given by

$$S_{\Phi}(\omega) = A_{\Phi}^2 \left( \frac{2\pi \times 1\text{Hz}}{|\omega|} \right) \quad (13)$$

where  $A_{\Phi}$  is the flux noise amplitude. Following the theory in [4], the flux noise dephasing rate away from the flux sweet spots can be expressed as

$$\Gamma_{\varphi R}^{\Phi} = \left| \frac{\partial \omega_{ge}}{\partial \Phi_{\text{ext}}} \right| A_{\Phi} \sqrt{\ln \left( \frac{1}{\omega_{\text{ir}} t} \right) + 1} \quad (14)$$

where  $\omega_{\text{ir}}$  is the low cut off frequency set by the duration of the Ramsey experiment and  $t$  is the free evolution decay time. The factor  $\sqrt{\ln(1/\omega_{\text{ir}} t + 1)}$  is measurement specific, however, we treat it as a constant in our case, as it remains approximately constant over the range of  $t$ . The green line in Fig. 3(e) of the main text refers to the expected Ramsey coherence times,  $T_{2R}^{\Phi}$ , from the flux noise contribution. The fitted flux noise amplitude,  $A_{\Phi}$ , is  $1.2 \times 10^{-4} \Phi_0 / \sqrt{\text{Hz}}$ .

### B. Dephasing from Aharonov-Casher noise

Aharonov-Casher noise arises from fluctuations in the qubit frequency caused by variations in  $E_{s,1}$  and  $E_{s,2}$  over time. As described in the main text, the variation in the phase slip rates stems from changes in the distribution of

offset charges along the wire. In this phenomenological model, we assume that the charge noise, which is typically modeled as a  $1/f$  Gaussian distributed noise, also leads to a  $1/f$  Gaussian distributed type noise in  $E_{s,1}$  and  $E_{s,2}$ . We can then express the dephasing rate from the AC noise in a similar manner to the dephasing rate from the flux noise. This is given by

$$\Gamma_{\varphi R}^{\text{AC}} = \left| \frac{\partial \omega_{ge}}{\partial E_{s,i}} \right| A_{\text{AC}} \sqrt{\ln \left( \frac{1}{\omega_{\text{ir}} t} \right) + 1} \quad (15)$$

where  $\partial \omega_{ge}/\partial E_{s,i}$  is the change in the qubit radian frequency with respect to a change in  $E_{s,1}$  or  $E_{s,2}$ . Fig. S6(a) and (b) below show the qubit frequency near zero flux for different values of  $E_{s,1}$  and  $E_{s,2}$ , respectively. In our experiment, we cannot distinguish between dephasing resulting from  $E_{s,1}$  and  $E_{s,2}$ . In the main text, we only consider the AC dephasing due to variations in  $E_{s,1}$  since it is the leading order term in the Hamiltonian. This results in an AC noise amplitude,  $A_{\text{AC}}$ , of  $0.037E_{s,1}/\sqrt{\text{Hz}}$ . It is possible that the charge noise could also lead to changes in  $E_{s,2}$ . In Fig. S6(c), we consider the Ramsey coherence time from AC noise due to changes in  $E_{s,2}$  only. From the fit, the AC noise amplitude is  $A_{\text{AC}2} = 0.090E_{s,2}/\sqrt{\text{Hz}}$ , while the flux noise amplitude increases slightly to  $A_{\Phi} = 1.4 \times 10^{-4}\Phi_0/\sqrt{\text{Hz}}$ .

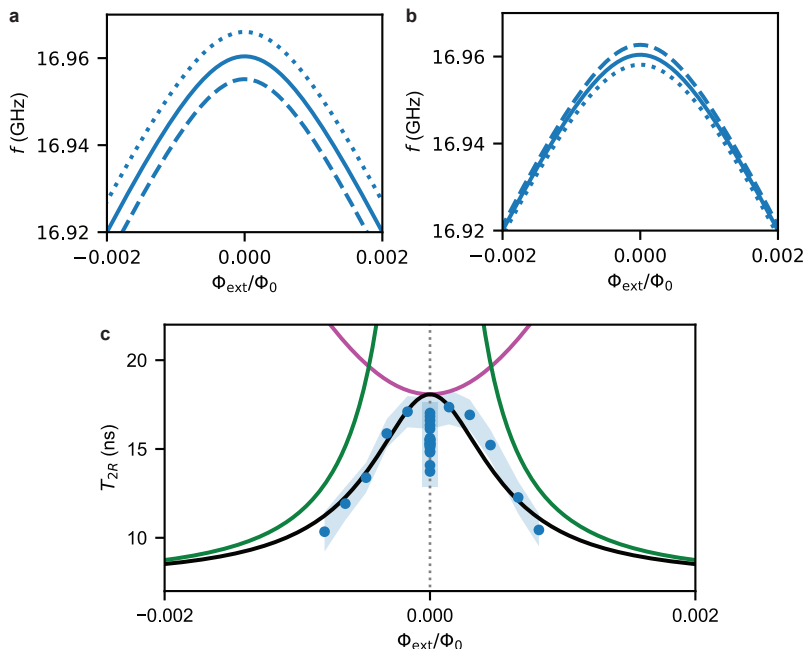


FIG. S6. **Simulated qubit frequencies and qubit coherence due to variations in  $E_{s,2}$ .** (a) Qubit frequency near zero flux when  $E_{s,1}$  is 0.93 GHz (dashed line), 1.03 GHz (solid line), and 1.13 GHz (dotted line) while keeping  $E_{s,2}$  constant at 0.050 GHz. (b) Qubit frequency near zero flux when  $E_{s,2}$  is 0.045 GHz (dashed line), 0.050 GHz (solid line), and 0.055 GHz (dotted line) while keeping  $E_{s,1}$  constant at 1.03 GHz. (c) Ramsey coherence time  $T_{2R}$  versus flux. The shaded region indicates the error from fitting the  $T_{2R}$  data. The green line shows the expected flux dependence of  $T_{2R}$  due to first-order flux noise dephasing with noise amplitude,  $A_{\Phi} = 1.4 \times 10^{-4}\Phi_0/\sqrt{\text{Hz}}$ . The pink line shows the Ramsey coherence time resulting from Aharonov-Casher dephasing for variations in  $E_{s,2}$  with noise amplitude,  $A_{\text{AC}2} = 0.090E_{s,2}/\sqrt{\text{Hz}}$ . The black line is expected limit from the quadrature sum of both models. The gray line is a guide for zero flux and the range of variations of  $T_{2R}$  in time is shown by the data points at zero flux. Note that at zero flux, only the point with the highest  $T_{2R}$  was included in the fit.

## VII. OPERATION OF QUBIT AT ELEVATED TEMPERATURES

### A. Extracting qubit temperature

During the mixing chamber temperature sweep, we perform qubit histogram measurements where we extract  $P_r$ , the ratio of the probability of the qubit being in state  $|e\rangle$  to the probability of the qubit being in state  $|g\rangle$ . We then use the Boltzmann distribution to calculate the qubit temperature.

$$T_{\text{qubit}} = \frac{-\hbar\omega}{k_B \ln(P_r)} \quad (16)$$

where  $\omega$  is the qubit radian frequency at zero flux.

### B. Temperature dependence of qubit lifetime

To model the decrease in  $T_1$  with increasing mixing chamber temperature, we assume that  $Q_{\text{ind}}$  changes to reflect the increase in the number of quasiparticles [5]:

$$\frac{1}{Q_{\text{ind}}(T)} = 2\alpha \sqrt{\frac{k_B T}{\pi \hbar \omega}} \exp\left(\frac{-\Delta_0}{k_B T}\right) + \frac{1}{Q_{\text{ind}}^{\text{initial}}} \quad (17)$$

In the expression above,  $\alpha = L_k/L_{\text{total}}$  is the kinetic inductance fraction, which is approximately one in our devices.  $\Delta_0 \approx 1.76k_B T_c$  is the superconducting gap of TiN at zero temperature, where we let  $T_c = 2.9$  K, extracted from separate independent measurements of kinetic inductance versus temperature. We also assume that the bath temperature remains the calculated qubit temperature at each mixing chamber temperature point in Eq.17 and Eq.10. We let  $Q_{\text{ind}}^{\text{initial}} = 5.0 \times 10^4$ , which is a slight adjustment from the fitted value near the zero flux flux sweep, to match the initial  $T_1 = 66 \mu\text{s}$  data point during the temperature sweep.

## VIII. DEVICE B MEASUREMENTS

### A. Qubit spectroscopy and time domain measurements of Device B at base mixing chamber temperature

To evaluate the reproducibility of the results, we performed measurements on another device (B). Although Device B is located in a different chip, both devices were designed to have the same parameters and have gone through the same fabrication process. In Fig. S7(a), we plot the two-tone spectroscopy data near zero flux for Device B. We were unable to perform two-tone spectroscopy close to the half-flux point due to a reduction in visibility of the resonator signal. Thus, we only fit the qubit Hamiltonian to the data near zero flux, which leads to a larger uncertainty in the phase slip rates compared to Device A. From the fit, we extract  $E_L = 35.1 \pm 0.1$  GHz,  $E_{s,1} = 0.9 \pm 0.9$  GHz, and  $E_{s,2} = 0.04 \pm 0.04$  GHz. The difference in  $E_L$ , and correspondingly the qubit frequency, between Device A and B is only  $\sim 3\%$ , which demonstrates the predictability of our qubits.

In Fig. S7 (b), we present the results of Device B's time domain measurements at zero flux. We find that the qubit lifetime with  $T_1 = 22 \mu\text{s}$  is lower than Device A's lifetime at zero flux, however, the coherence time is slightly higher with  $T_{2R} = 20$  ns.

### B. Device B time domain measurements at elevated temperature

We also investigate the operation of Device B at elevated temperatures. We raise the temperature of the mixing chamber to 200 mK and perform time-domain measurements. We find that the qubit lifetime and coherence times are relatively unaffected at this temperature (See Fig. S8).

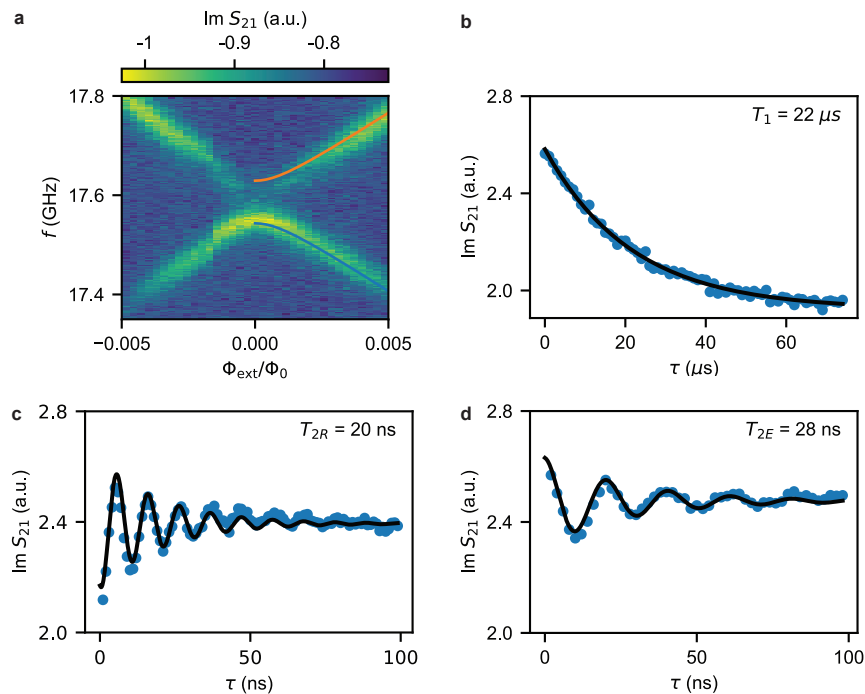


FIG. S7. **Device B qubit spectroscopy and time domain measurements** (a) Two-tone spectroscopy near zero flux. The fit to the  $|g\rangle - |e\rangle$  transition (blue line) and  $|g\rangle - |f\rangle$  transition (orange line) is shown on the right half of the data. (b-d) Time domain measurements taken at zero flux measuring (b) the relaxation time,  $T_1$ , (b) the Ramsey coherence time,  $T_{2R}$ , and (c) the coherence time with the application of an echo pulse,  $T_{2E}$ .

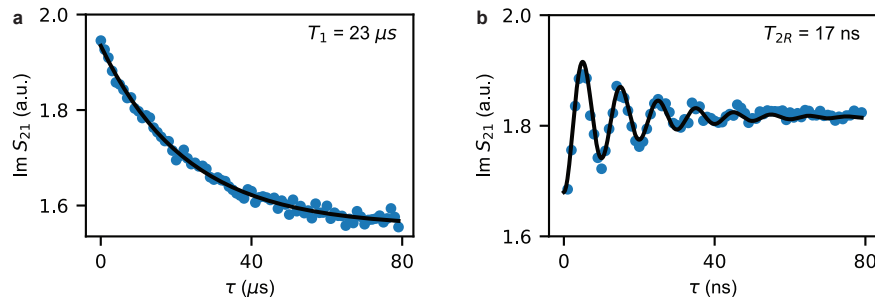


FIG. S8. **Device B time domain measurements at 200 mK** (a) Measurement of relaxation time,  $T_1$ . (b) Measurement of Ramsey coherence time,  $T_{2R}$ . Neither  $T_1$  nor  $T_{2R}$  changes significantly compared to measurements conducted at base temperature.

- 
- [1] J. Johansson, P. Nation, and F. Nori, QuTiP 2: A Python framework for the dynamics of open quantum systems, *Computer Physics Communications* **184**, 1234 (2013).
- [2] W. C. Smith, A. Kou, X. Xiao, U. Vool, and M. H. Devoret, Superconducting circuit protected by two-Cooper-pair tunneling, *npj Quantum Information* **6**, 1 (2020).
- [3] M. T. Randeria, T. M. Hazard, A. Di Paolo, K. Azar, M. Hays, L. Ding, J. An, M. Gingras, B. M. Niedzielski, H. Stickler, J. A. Grover, J. L. Yoder, M. E. Schwartz, W. D. Oliver, and K. Serniak, Dephasing in Fluxonium Qubits from Coherent Quantum Phase Slips, *PRX Quantum* **5**, 030341 (2024).
- [4] G. Ithier, E. Collin, P. Joyez, P. J. Meeson, D. Vion, D. Esteve, F. Chiarello, A. Shnirman, Y. Makhlin, J. Schrieffer, and G. Schön, Decoherence in a superconducting quantum bit circuit, *Physical Review B* **72**, 134519 (2005).
- [5] K. R. Amin, C. Ladner, G. Jourdan, S. Hentz, N. Roch, and J. Renard, Loss mechanisms in TiN high impedance superconducting microwave circuits, *Applied Physics Letters* **120**, 164001 (2022).